

Dissecting the Extended Main Sequence Turn-off of the Young Star Cluster NGC 1850[★]

Matteo Correnti^{1†}, Paul Goudfrooij¹, Andrea Bellini¹, Jason S. Kalirai^{1,2}
and Thomas H. Puzia³

¹*Space Telescope Science Institute, 3700 San Martin Drive, Baltimore, MD 21218, USA*

²*Center for Astrophysical Sciences, 3400 N. Charles Street, John Hopkins University, Baltimore, MD 21218, USA*

³*Institute of Astrophysics, Pontificia Universidad Católica de Chile, Av. Vicuña Mackenna 4860, Macul 7820436, Santiago, Chile*

Accepted 2016 December 20. Received 2016 December 12; in original form 2016 November 07

ABSTRACT

We use the Wide Field Camera 3 onboard the *Hubble Space Telescope* to obtain deep, high-resolution photometry of the young (~ 100 Myr) star cluster NGC 1850 in the Large Magellanic Cloud. We analyze the cluster colour-magnitude diagram (CMD) and find that it hosts an extended main-sequence turn-off (MSTO) and a double MS. We demonstrate that these features cannot be due to photometric errors, field star contamination, or differential reddening. From a comparison with theoretical models and Monte Carlo simulations, we show that a coeval stellar population featuring a distribution of stellar rotation rates can reproduce the MS split quite well. However, it *cannot* reproduce the observed MSTO region, which is significantly wider than the simulated ones. Exploiting narrow-band H α imaging, we find that the MSTO hosts a population of H α -emitting stars which are interpreted as rapidly rotating Be-type stars. We explore the possibility that the discrepancy between the observed MSTO morphology and that of the simulated simple stellar population (SSP) is caused by the fraction of these objects that are highly reddened, but we rule out this hypothesis. We demonstrate that the global CMD morphology is well-reproduced by a combination of SSPs that cover an age range of ~ 35 Myr *as well as* a wide variety of rotation rates. We derive the cluster mass and escape velocity and use dynamical evolution models to predict their evolution starting at an age of 10 Myr. We discuss these results and their implications in the context of the extended MSTO phenomenon.

Key words: galaxies: star clusters — globular clusters: general — Magellanic Clouds

1 INTRODUCTION

Deep colour-magnitude diagrams (CMDs) from images taken with the Advanced Camera for Survey (ACS) and the Wide Field Camera 3 (WFC3) onboard the *Hubble Space Telescope* (*HST*) revealed that several intermediate-age (~ 1 – 2 Gyr) star clusters in the Magellanic Clouds host extended main-sequence turn-off (MSTO) regions (Mackey et al. 2008a; Glatt et al. 2008; Milone et al. 2009; Goudfrooij et al. 2009, 2011b, 2014; Correnti et al. 2014), in some cases accompanied by composite red clumps (Girardi et al. 2009; Rubele et al. 2011). The presence of these extended MSTOs (hereafter eMSTOs) has been in-

terpreted as due to stars that formed at different times within the parent cluster, with age spreads of 150–500 Myr (Milone et al. 2009; Girardi et al. 2009; Rubele et al. 2010, 2011; Goudfrooij et al. 2011b, 2014; Keller et al. 2012; Correnti et al. 2014). If so, these objects might be the younger counterparts of the old Galactic globular clusters with multiple stellar populations (e.g., Conroy & Spergel 2011). An alternative scenario to explain the eMSTO phenomenon was originally proposed by Bastian & de Mink (2009), who suggested that this is due to the presence of a spread in rotation velocity among turn-off stars (for a detailed discussion, see Girardi et al. 2011; Goudfrooij et al. 2014; Niederhofer et al. 2015; Brandt & Huang 2015, and references therein). Finally, Yang et al. (2011) suggested that the eMSTOs and the dual clumps can be photometric features produced by merged binary systems and interacting binaries with mass transfer.

Recently, eMSTOs have been detected also in young

[★] Based on observations with the NASA/ESA *Hubble Space Telescope*, obtained at the Space Telescope Science Institute, which is operated by the Association of Universities for Research in Astronomy, Inc., under NASA contract NAS5-26555

[†] E-mail: correnti@stsci.edu

(~ 100 – 300 Myr) massive star clusters in the Large Magellanic Cloud (LMC). In particular, [Milone et al. \(2015a\)](#) and [Correnti et al. \(2015, hereafter C15\)](#) discovered the presence of an eMSTO in the star cluster NGC 1856, consistent with the presence of an age spread of ~ 80 Myr. Interestingly, the CMD of NGC 1856 also shows a split in the MS ([Milone et al. 2015a](#)), which has been interpreted as an indication that the cluster might host two coeval stellar populations with different rotational velocities ([D’Antona et al. 2015](#)). [Milone et al. \(2016a\)](#) found that the CMD of the young (~ 100 Myr) star cluster NGC 1755 shows a similar morphology, including an eMSTO and a MS split. They demonstrated that the bimodal MS is well reproduced by a single stellar population with different rotation velocities, whereas the fit between the observed eMSTO and models with different rotation is not fully satisfactory. On the other hand, [Milone et al. \(2013\)](#) showed that the ~ 300 Myr cluster NGC 1844 presents only a split in the MS and not an eMSTO. It is evident that these new discoveries in young clusters give us a new opportunity to study the nature of the eMSTO phenomenon and to provide additional constraints to discriminate among the different scenarios.

In this context, another interesting object is the young (~ 100 Myr) star cluster NGC 1850 in the LMC. [Bastian et al. \(2016\)](#) used *HST* WFC3 observations with the *F336W* and *F438W* filters to show that the cluster hosts an eMSTO which can be reproduced by an age spread of ~ 40 Myr. However, they suggest that this is the age range expected when the effect of rotation in MSTO stars is interpreted in terms of an age spread, and thus concluded that no age spread is present in the cluster. They also suggest that the presence of an age spread should cause a “bimodal” distribution in the MSTO region, whereas the observed distribution can be approximated by a single (possibly skewed) Gaussian distribution¹.

Here, we present an analysis of new *HST* WFC3 photometry of NGC 1850, exploiting a different set of filters with respect to that used by [Bastian et al. \(2016\)](#). Our data, thanks to a significantly larger colour baseline, allow us to study thoroughly the CMD morphology and to perform a detailed analysis of the MSTO region. We compare the cluster CMD with theoretical models, using isochrones with different ages and different rotation rates and with Monte Carlo simulations in order to quantify to what extent the CMD can be reproduced by a simple stellar population (SSP) with a distribution of rotation rates. We derive the cluster mass and escape velocity to test whether the cluster has (or has had) the right properties to retain mass-loss material that can be (or could have been) used to form a second generation of stars. This study allows us to have a clearer picture of the cluster’s star formation history and in particular on the nature of the observed eMSTO region.

The remainder of the paper is organized as follows: observations and data reduction are presented in Section 2. In Section 3, we discuss the observed CMD, whereas in Section 4 we compare the observed CMD with theoretical models, using isochrones with different ages and different rotation rates. In Section 5, we compare the observed CMD with Monte Carlo simulations, both using one SSP with different

rotation rates and a combination of four SSPs with different ages and different rotation rates; we obtain the pseudo-colour distributions for the observed and simulated CMDs and compare them. In Section 6, we present the analysis of narrow-band $H\alpha$ imaging. In Section 7, we investigate how the CMD morphology changes as a function of the distance from the cluster center, while the physical and dynamical properties of the cluster are presented in Section 8. Finally, in Section 9, we discuss our results and their implications on the interpretation of the eMSTO phenomenon.

2 OBSERVATIONS AND DATA REDUCTION

NGC 1850 was observed with *HST* on 2015 October 22 using the UVIS channel of the WFC3 as part of the *HST* program 14174 (PI: P. Goudfrooij). The cluster was centered on one of the two CCD chips of the WFC3/UVIS camera, to avoid the loss of its central region due to the CCD chip gap and to minimize the impact of different photometric zeropoints for the two chips. The cluster was observed using three filters, namely *F275W*, *F656N*, and *F814W*. Two long exposures were taken in the *F275W* and *F814W* filters, and three in the *F656N* filter. The total exposure times for each filter are 1570 s (*F275W*), 2875 s (*F656N*), and 790 s (*F814W*). In addition, we took two short exposures in the *F275W* and *F814W* filters (150 s and 10 s, respectively), to avoid saturation of the brightest stars. The two or three long exposures were spatially offset from each other by $0''.18$ and $-2''.401$ in a direction $+85^\circ.76$ with respect to the positive X- and Y-axis of the detector. This was done to move across the gap between the two WFC3/UVIS CCD chips, as well to simplify the identification and removal of hot pixels. To investigate the $H\alpha$ -emitting stars in the cluster, we complemented our dataset with archival observations with the filter *F467M* (GO-11925, PI: S. E. Deustua). The main purpose of this filter in this context is to define the continuum level at the wavelength of $H\alpha$ along with the *F814W* filter. Program GO-11925 is a calibration program to test the linearity of WFC3/UVIS, hence images in this filter were taken with various exposure times; for our purpose, only the two long exposures were useful (300 s and 500 s, respectively). In addition to the WFC3/UVIS observations, we used the Wide Field Camera (WFC) of ACS in parallel to obtain images $\sim 6'$ from the cluster center using the *F555W*, *F658N*, and *F814W* filters. These observations provide a clean picture of the stellar content, star formation history, and $H\alpha$ -emitting stars in the underlying LMC field.

To reduce the images, we use the following method. Briefly, we start from the *flt* files provided by the *HST* pipeline, which constitute the bias-corrected, dark-subtracted, and flat-fielded images. The *flt* files are first corrected for charge transfer inefficiency effects using the dedicated CTE correction software². Star positions and fluxes are measured on the CTE-corrected *flc* files using the publicly-available FORTRAN program *img2xym_wfc3uv* with the available library of spatially variable point-spread functions (PSFs, in an array of 7×8 PSFs) for each filter. We derive an additional 5×5 array of perturbation PSFs

¹ This suggestion will be addressed in Sect. 5.

² http://www.stsci.edu/hst/wfc3/tools/cte_tools

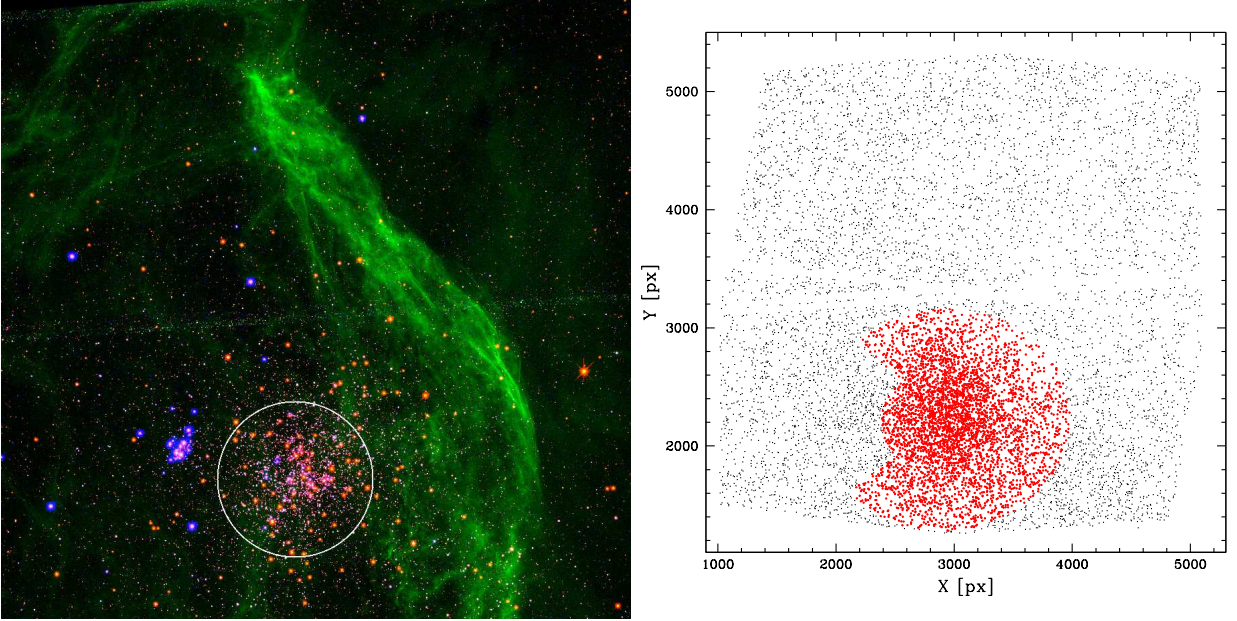


Figure 1. Left panel: stacked trichromatic image of the WFC3/UVIS field (red channel: $F814W$ filter; green channel: $F656N$ filter; blue channel: $F275W$ filter). The white circle marks a region of $\approx 20''$ which corresponds to the cluster effective radius r_e . The young cluster NGC 1850B is clearly visible on the left side of the cluster as well as the gas filaments that stretch from the upper-left corner to the bottom-right corner, covering a large portion of the image. Right panel: XY spatial distribution for all the stars in the WFC3/UVIS field of view. Stars inside the region considered as the cluster field in our analysis are reported as red dots. The annulus segment on the left side has been excluded, in order to avoid contamination by young stars belonging to NGC 1850B.

for each exposure, to account for telescope breathing effects (Bellini et al. 2014), and we combine it with the library PSFs to fit stellar profiles. Stellar positions are corrected for geometric distortion using the solution provided by Bellini et al. (2011). Then, we create a master-frame list using one of the $F814W$ exposures and we transform and average the exposures for the other filters into the reference system defined by the master frame by means of a six-parameter linear transformation. To obtain the final catalog we use the FORTRAN software package KS2 (J. Anderson, in preparation). This program allows us to find and measure stars in all the individual exposures simultaneously and in particular to measure faint objects that cannot be detected in individual exposures. Photometry of saturated stars is measured following the method developed by Gilliland (2004) for the ACS camera and subsequently demonstrated to be valid also for the WFC3/UVIS detector (Gilliland et al. 2010), which allows one to recover the electrons that have bled into neighbouring pixels.

To obtain the photometric calibration, we compare PSF-based instrumental magnitudes measured on the *flc* exposures with aperture-photometry magnitudes measured on the *drc* exposures (i.e., the distortion-corrected and resampled *flc* files) using a fixed aperture of 10 pixels. We then transform the magnitudes into the VEGAMAG system by adopting the relevant synthetic zero-points³. Finally, for our analysis we select only those sources that are recovered in both exposures for the filters $F275W$, $F467M$, and $F814W$, and in two out of three exposures for the filter $F656N$, and we clean the obtained catalog using the quality-of-fit (QFIT)

parameter, provided by KS2, which identifies how well a source has been fit with the PSF model (Anderson et al. 2008).

Completeness as well as the photometric-error distribution of the final photometry are characterized by performing artificial star tests. We use the standard technique of adding artificial stars to the images and running them through the photometric routines applied in the reduction process. The method adopted to perform the artificial star tests is described in Anderson et al. (2008). Briefly, we generate a list of 3×10^5 artificial stars and we distribute them in magnitude in order to reproduce a luminosity function similar to the observed one and with a colour distribution that span the full colour ranges found in the CMDs. The overall distribution of the inserted artificial stars follows that of the stars in the image. Each star in the list is inserted one at a time in the images with the appropriate flux and position and it is measured using the same procedure and PSF adopted for real stars. We consider the inserted stars recovered if the input and output magnitudes agree to within 0.75 mag in every filter and if the input and output position agree to within 0.5 pixel. Finally, a completeness fraction is assigned to each individual star in a given CMD as a function of its magnitude and distance from the cluster center.

The left panel of Fig. 1 shows a trichromatic stacked image of the WFC3/UVIS field of view (red channel: $F814W$ filter; green channel: $F656N$ filter; blue channel: $F275W$ filter). The white circle has a radius of $\approx 20''$ which corresponds to the effective radius r_e of the cluster, as derived in Sect. 8.1. On the left side of NGC 1850, the much younger cluster NGC 1850B is clearly visible. The stacked image nicely outlines the gas filaments which cover a large portion of the

³ http://www.stsci.edu/hst/wfc3/analysis/uviss_zpts

UVIS field of view. However, as derived in Sect. 3.2, these filaments seem to lie behind the cluster and therefore do not affect our analysis. In the following, we define the region enclosed within a radius of $2 \times r_e$ as “the cluster field”. In order to minimize the contamination from the stars belonging to NGC 1850B, we excluded from the final “NGC 1850 field” catalog objects in the annular segment in the direction of NGC 1850B (i.e., the stars that have a position angle between 138° and 217° in the detector frame and for which the distance from the cluster center is larger than r_e). In the right panel of Fig. 1, we show the spatial positions of the selected stars in the field of view. The objects that satisfy the aforementioned criteria and represent the NGC 1850 cluster field are reported as red dots.

3 COLOUR-MAGNITUDE DIAGRAM ANALYSIS

3.1 A wide MSTO region and a MS split

Fig. 2 shows the $F814W$ vs. $F275W - F814W$ CMD of the NGC 1850 field, derived as described in Sect. 2 and reported in the right panel of Fig. 1. The observed CMD presents two interesting features: (1) a MSTO region that is wider than what is expected from a single stellar population and (2) the presence of two MSes: a blue and poorly-populated MS, and a red MS, which contains the majority of the stars. The two sequences run parallel from $F814W \sim 18.5$ mag to $F814W \sim 21.25$ mag, where they seem to merge together. The presence of a small colour difference between the two sequences at fainter luminosity, not detectable due to photometric errors, can however not be excluded. We calculate the ratio of stars in the blue and the red MSes by carefully selecting stars in the two MSes in a fixed magnitude interval ($19.5 \text{ mag} < F814W < 21.0$). We derive that the less-populated blue MS contains around 25% of stars, with the remaining 75% belonging to the red MS (see Sect. 7 for a detailed discussion). This ratio is very similar to the one found by Milone et al. (2015a) for NGC 1755.

To verify that the observed broadening of the MSTO and the double MS are “real” features in the cluster CMD, we checked for the following potential causes: contamination by field stars, photometric errors, and differential reddening.

We assess the level of contamination by the field population by selecting a region near the top-right corner of the image which has the same surface area as the cluster field. The stars in this region are shown in Fig. 2 as red open squares. Note that these stars mainly contaminate the lower MS, at fainter magnitudes than the observed splitting, and they do not affect the MSTO at all. We therefore conclude that field stars are not the cause of the observed split in the MS and the broadening in the MSTO region.

Photometric uncertainties are derived during the reduction process. Magnitude and colour errors are shown in the left panel of Fig. 2; photometric errors at the MSTO level are ≈ 0.005 mag, whereas they are of the order of 0.015 mag at a magnitude $F814W \sim 21.5$ mag, where the MSes are clearly separated. These errors are far too small to account for the observed broadening of the MSTO.

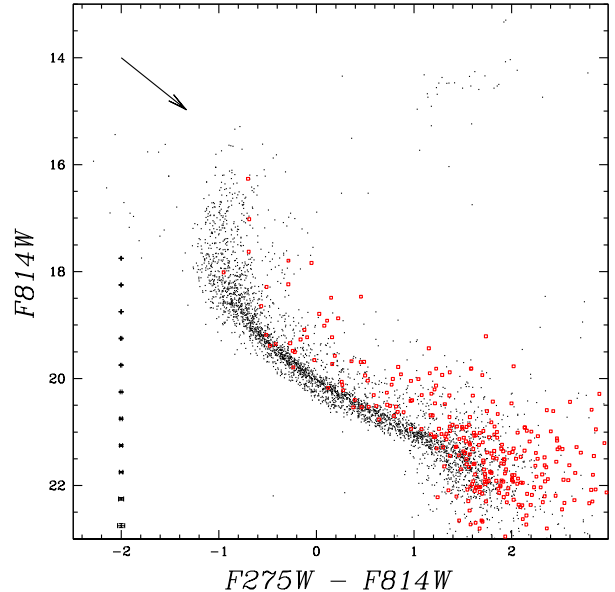


Figure 2. Observed $F814W$ vs. $F275W - F814W$ CMD for all the stars inside the NGC 1850 field, defined in Sect. 2 and shown in the right panel of Fig. 1. We determine the contamination from the underlying LMC field population from a region, with the same surface area adopted for the cluster star, near the top-right corner of the image. Stars located in this region are superposed on the cluster CMD (red squares). Magnitude and colour errors are shown in the left side of the CMD. The reddening vector is also shown for $A_V = 0.5$.

3.2 The impact of differential reddening

To check whether differential reddening is present in our WFC3/UVIS field of view and, in particular, in the cluster region, we adopt the same approach as in Correnti et al. (2015) and described in detail in Milone et al. (2012). Briefly, we first rotate the CMD to a photometric reference frame in which the X-axis is parallel to the reddening line. This reference system makes it easier to estimate reddening differences than in the original colour-magnitude plane, where the reddening vector is inclined. Then, we generate a fiducial line along the most-populated red MS and, among the stars in the red MS, we select a sample of reference stars with high-precision photometry. For each star in the field of view, we select a sample of 50 neighbour reference stars and we calculate the residual colours with respect to the fiducial line. The median of these residuals, calculated along the reddening direction, is assumed as the differential reddening corresponding to each star. Each reference star is excluded in the computation of its own differential reddening.

The results of the differential reddening correction are shown in Fig. 3, where we compare a zoom-in portion of the MS for the original CMD (left panel) of NGC 1850 and the CMD corrected for differential reddening (middle panel). The two CMDs are almost identical, suggesting that the impact of differential reddening is negligible and that the MS split is real. As a further proof, we show in the right panel of Fig. 3 the spatial distribution of the differential reddening in our field of view. Each star is reported with a different colour, depending on the final $\Delta E(B - V)$ that we applied.

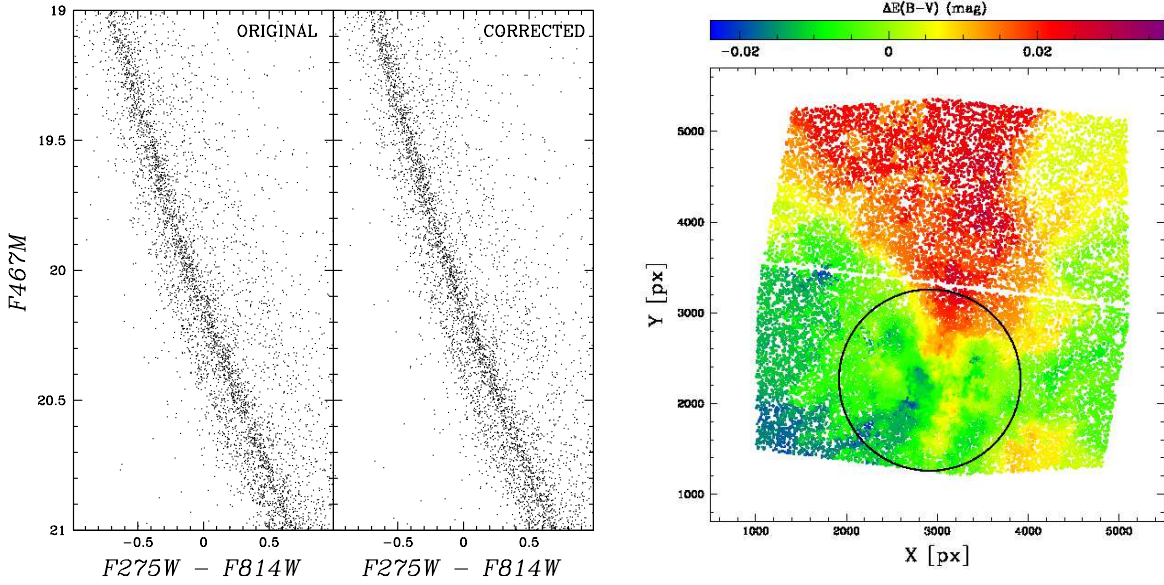


Figure 3. Left panels: Original F_{467M} vs. $F_{275W} - F_{814W}$ CMD of stars in the NGC1850 field of view, and CMD corrected for differential reddening, both zoomed in the central part of the MS. Right panel: Spatial distribution of the differential reddening in the WFC3/UVIS field of view. The colour of each star represents the final $\Delta E(B-V)$ derived from the differential reddening correction. The colour coding is shown at the top. The black circle marks a diameter of $\approx 40''$ (i.e. $2 \times r_e$).

In order to better visualize how the differential reddening impacts the area of the cluster field, we report in Fig. 3 a circular region, with a radius $r = 2 \times r_e$. Fig. 3 clearly shows that the reddening variations in the NGC 1850 field are very small, of the order of ± 0.02 mag in $E(B-V)$. The technique that we applied is able to minimize the amount of differential reddening in the foreground of the cluster. We find a very small reddening variation across the field of view, and with a very specific spatial pattern that is completely uncorrelated to the $H\alpha$ filaments we see in Fig. 1. This implies that these filaments are located behind the cluster. Finally, since the reddening variation is negligible, we use the original photometry in the analysis for simplicity.

4 ISOCHRONE FITTING

To understand the nature of the double MS and extended MSTO in NGC 1850, we compare the CMD with model isochrones. We investigate the possibility that these features are caused by the two main scenarios presented in the literature: the presence of an age spread in the cluster or of a range of rotation velocities among the cluster stars.

Isochrone fitting is performed following the method described in detail in Goudfrooij et al. (2011b), and adopted also in C15, for the case of star clusters that do not yet have a developed RGB.

In the following Sections, we show the results of the isochrone fitting for the two aforementioned scenarios.

4.1 Isochrones fitting: age spread

To test whether an age spread can reproduce the observed CMD morphology, we superpose two isochrones from PAR-

SEC (Bressan et al. 2012) of different age (~ 90 Myr and ~ 60 Myr) on the F_{814W} vs. $F_{275W} - F_{814W}$ CMD shown in the left panel of Fig. 4 (red and blue lines, respectively). The age of the isochrones are chosen to match the maximum and minimum age that can be accounted for by the position and width of the MSTO. Note (a) that the morphology of the MSTO is not very well reproduced by a SSP and that an age spread of the order of 30 Myr may constitute a better fit to the data in this region of the CMD and (b) that the observed double MS cannot be reproduced at all using a combination of different ages. Interestingly, we note that if we adopt the same parameters in terms of age, metallicity, distance, and reddening and we superpose the isochrones in the F_{467M} vs. $F_{467M} - F_{814W}$ CMD (shown in the right panel of Fig. 4) we see that the selected isochrones do not fit the CMD MS, the isochrones being too red with respect to the observed MS (note that due to the shorter colour baseline, the split is not observable in this CMD).

To verify that this discrepancy is not due to systematic uncertainties in the isochrone colour transformations, we also perform the inverse approach. We use the F_{467M} vs. $F_{467M} - F_{814W}$ CMD (left panel of Fig. 5) to derive the isochrone parameters and then we overplot them onto the F_{814W} vs. $F_{275W} - F_{814W}$ CMD (right panel of Fig. 5). The latter CMD shows that also in this case a combination of isochrones with different ages provides a satisfactory fit of the MSTO. And, importantly, *both isochrones match the less-populated blue MS of the cluster very well*. This is a clear indication that the red MS, containing the majority of stars, cannot be reproduced using non-rotating isochrones with different ages and thus *must be constituted by rotating stars*.

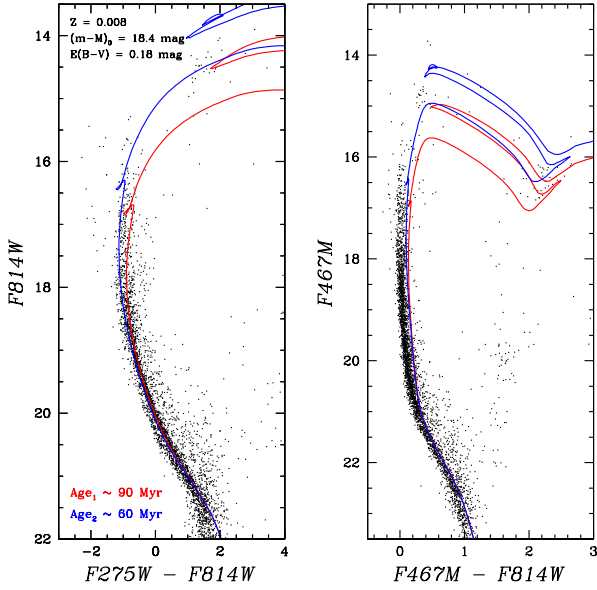


Figure 4. Left panel: $F814W$ vs. $F275W - F814W$ CMD for NGC 1850. Best-fitting isochrones from PARSEC (Bressan et al. 2012), for the minimum (blue line) and maximum (red line) age (~ 60 and ~ 90 Myr, respectively) that can be accounted for by the data are superposed on the cluster CMD, along with the derived metallicity, distance modulus $(m-M)_0$ and reddening $E(B-V)$. Right panel: $F467M$ vs. $F467M - F814W$ CMD. Isochrones with the same parameters as in the left panel are overlaid on the cluster CMD.

4.2 Isochrones fitting: range of rotation velocities

As mentioned above, the alternative scenario proposed to explain the eMSTO phenomenon suggests that it is caused by a spread in rotation velocity among TO stars. To test this scenario, we use the isochrones from the Geneva SYCLIST database (Ekström et al. 2012; Georgy et al. 2013, 2014) for which different rotation rates are available. The left panel of Fig. 6 shows the $F814W$ vs. $F275W - F814W$ CMD with superimposed the isochrones for different rotation rates. In detail, the red isochrone has no rotation, i.e. $\Omega/\Omega_{crit} = 0.0$, where Ω_{crit} represents the critical (break-up) rotation rate, whereas isochrones with $\Omega/\Omega_{crit} = 0.30, 0.50, 0.80, 0.90,$ and 0.95 are reported in magenta, yellow, green, cyan, and blue, respectively. The non-rotating isochrone has been extended to masses $M < 1.7 M_{\odot}$ by using the models of Mowlavi et al. (2012, reported in the CMD as a red dashed line). Due to slightly different input physics in the two models, a small color mismatch is present between the two non-rotating isochrones. To account for it, we shifted the Mowlavi et al. (2012) non-rotating isochrone toward the blue by 0.06 mag. Rotating isochrones with $M < 1.7 M_{\odot}$ are not (yet) available. The adopted age, distance modulus, and reddening are also reported in the left panel of Fig. 6. For what concerns metallicity, only three options are provided by the Geneva database for the rotating isochrones and we choose the value most appropriate for our case (i.e., $Z = 0.006$).

A combination of different rotation rates seems to reproduce the MS split and the distribution of stars in the blue loop quite well. In particular, fast-rotating stars ($\Omega/\Omega_{crit} >$

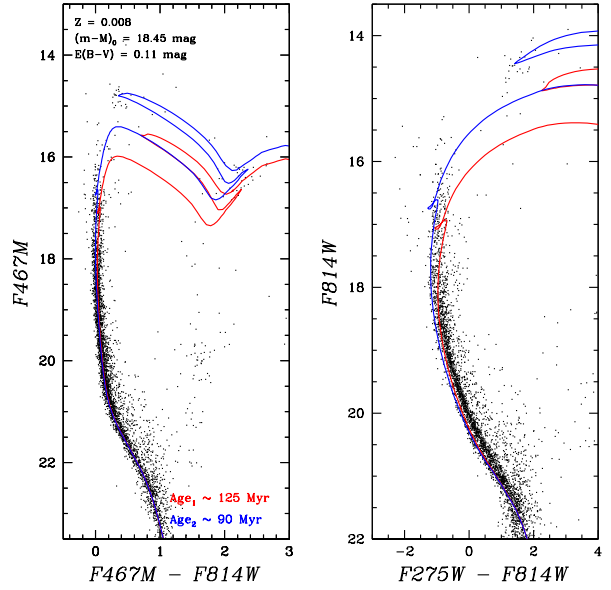


Figure 5. Similar to Fig. 4. In this case, best-fitting isochrones are derived from the $F467M$ vs. $F467M - F814W$ CMD (left panel). The adopted age, metallicity, distance, and reddening are also reported. Isochrones with these values are superimposed on the $F814W$ vs. $F275W - F814W$ CMD (right panel).

0.80) constitute the more populated red MS, whereas non-rotating/slow rotating stars ($\Omega/\Omega_{crit} < 0.50$) constitute the blue MS. The presence of a clear gap between the two MSes and thus the absence of intermediate-velocity rotators ($0.50 < \Omega/\Omega_{crit} < 0.80$) indicates that the distribution of rotation velocities is somewhat bimodal, rather than continuous. Fig. 6 also shows that the fit in the MSTO is not satisfactory. This can be better appreciated in the right panels of Fig. 6, in which we show zoom-in views of the MSTO (top panel) and the MS in the surroundings of the split (bottom panel). In particular, in the MSTO region, while the “spread” in $F814W$ magnitude is reproduced by a combination of isochrones of different rotation rates, the spread in colour is larger in the observed CMD with respect to the one produced by the isochrones. This is further addressed below.

5 MONTE CARLO SIMULATIONS

To further determine to what extent a range in rotation velocities can reproduce the observed CMD, and in particular the observed MSTO morphology, we conduct Monte Carlo simulations of synthetic clusters with a single age and different stellar rotation velocities (the method adopted to produce these simulations is described in detail in Goudfrooij et al. 2011b, 2014). Briefly, we simulate a SSP with a given age and chemical composition populating the non-rotating and rotating isochrones. Stars are randomly drawn using a Salpeter mass function and normalized to the observed (completeness-corrected) number of stars. As a first guess, we arbitrarily populated the different isochrones, in terms of Ω/Ω_{crit} , such that the relative numbers of stars re-

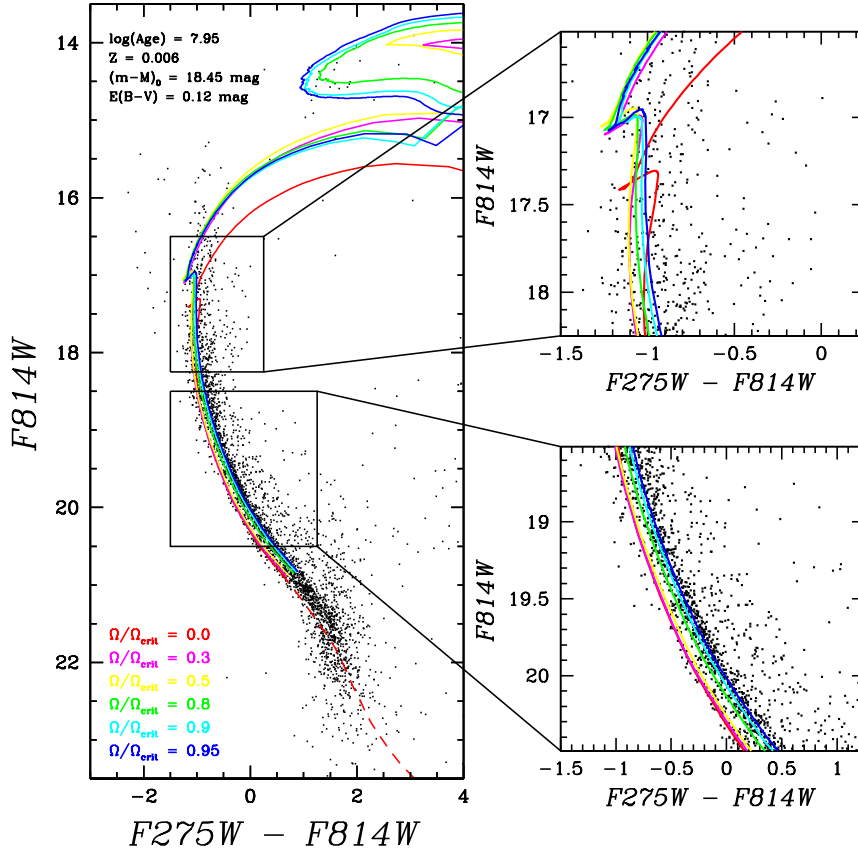


Figure 6. Left panel: $F814W$ vs. $F275W - F814W$ CMD with superimposed isochrones with different rotation rates from the Geneva database. Isochrones are colour-coded, in terms of their Ω/Ω_{crit} , as follows: $\Omega/\Omega_{crit} = 0.00$ (no rotation), red line; $\Omega/\Omega_{crit} = 0.30$, magenta line; $\Omega/\Omega_{crit} = 0.50$, yellow line; $\Omega/\Omega_{crit} = 0.80$, green line; $\Omega/\Omega_{crit} = 0.90$, cyan line, and $\Omega/\Omega_{crit} = 0.95$, blue line. Non-rotating isochrone, from Mowlavi et al. (2012), for $M < 1.7 M_{\odot}$ is shown as a dashed red line. Adopted age, metallicity, distance, and reddening are also reported. Right panels: zoom-in of the MSTO region (top panel) and of the MS (bottom panel) with superimposed the same isochrones as in the left panel.

flect the distribution of Ω/Ω_{crit} for A-type stars in the solar neighbourhood from Royer et al. (2007). After inspection of the results, we modified the relative numbers of stars so as to better reproduce the observed CMD morphology, that is to match the observed ratio between the blue and the red MS (i.e., we increased the relative numbers of stars for the fast-rotating populations with $\Omega/\Omega_{crit} \geq 0.80$). The adopted final values are the following: $\approx 10\%$ for $\Omega/\Omega_{crit} = 0.00$, $\approx 5\%$ for $\Omega/\Omega_{crit} = 0.30$, $\approx 10\%$ for $\Omega/\Omega_{crit} = 0.50$, $\approx 35\%$ for $\Omega/\Omega_{crit} = 0.80$, $\approx 30\%$ for $\Omega/\Omega_{crit} = 0.90$, and $\approx 10\%$ for $\Omega/\Omega_{crit} = 0.95$. A component of unresolved binary stars, derived from the same mass function, is added to a fraction of the sample stars. We use a flat distribution of primary-to-secondary mass ratios and we adopt a binary fraction of $\approx 40\%$. For the purposes of this work, the results do not change significantly within $\pm 20\%$ of the binary fraction. Finally, we add photometric errors with a distribution derived during the photometric reduction process. We also obtained SYCLIST cluster simulations from their website for comparison purposes. Simulations include gravity and limb darkening effects (Espinosa Lara & Rieutord 2011; Claret 2000) as well as a random distribution of inclination angles (rotation

velocity distribution from Huang et al. 2010). We found that the MSTO morphologies of the two sets of simulations are fully consistent with one another (see Sect. 5.1 below and right panel of Fig. 7). We derive four different sets of synthetic CMDs, with the only difference being the adopted age. In particular, we simulate four SSPs with $\log(\text{age})$ values of 7.95, 8.00, 8.05, and 8.10.

To compare in detail the observed MSTO region with the simulated ones, we create pseudo-colour distributions. Briefly, we construct a parallelogram across the MSTO (shown in the left panel of Fig. 7) and we select the stars within it. We define the distributions with the term ‘‘pseudo-colour’’ because it reflects the star distribution along the major axis of the parallelogram, rather than the $F275W - F814W$ colour. Then, we calculate the pseudo-colour distributions using the non-parametric Epanechnikov-kernel density function (Silverman 1986). This is done to avoid possible biases that can arise if fixed bin widths are used. We apply the procedure to both the observed and the simulated CMD. The results obtained from the comparison of the observed and simulated pseudo-colour distributions are described in the following Sections.

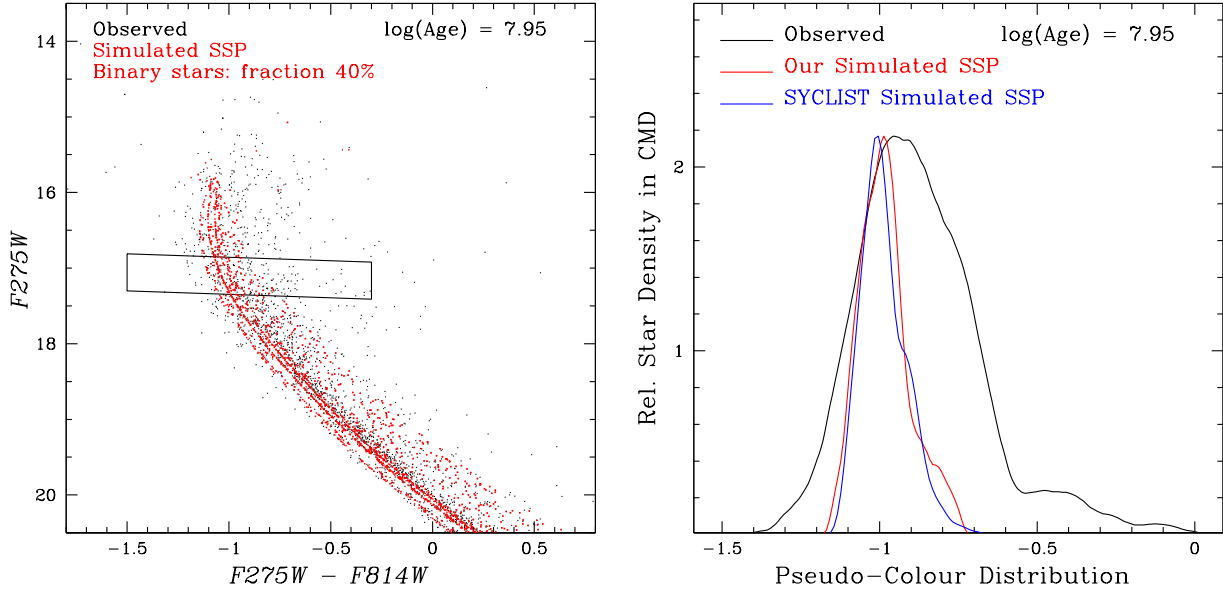


Figure 7. Left panel: comparison between observed (black dots) and simulated (red dots) CMDs. The latter is obtained from Monte Carlo simulations of a SSP with an age of ~ 90 Myr ($\log(\text{age}) = 7.95$), populating non-rotating and rotating isochrones as described in Sect. 5. We also report the parallelogram box used to select MSTO stars. Right panel: pseudo-colour distribution for the MSTO region of the observed (black line) and simulated (red line, our simulation; blue line, SYCLIST simulation) CMDs.

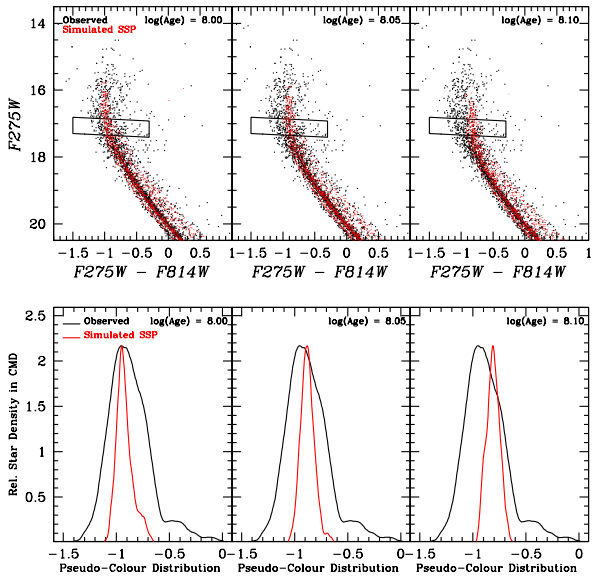


Figure 8. Top panels: comparison between the observed and simulated CMDs, obtained from SSP with ages $\log(\text{age}) = 8.00$ (left panel), $\log(\text{age}) = 8.05$ (middle panel), and $\log(\text{age}) = 8.10$ (right panel). Bottom panels: correspondent pseudo-colour distributions for the MSTO regions.

5.1 Testing the influence of stellar rotation at the MSTO

The left panel of Fig. 7 compares the observed and simulated CMD, the latter obtained as described above, adopting a sin-

gle SSP with an age of ~ 90 Myr ($\log(\text{age}) = 7.95$) and a distribution of rotation rates that fits the morphology of the MS split. As expected from the isochrone comparison described in the previous Section, this simulation reproduces the MS split quite well. Conversely, the MSTO region of the simulation does not reproduce the observed MSTO region well, the latter being wider than the former. This is highlighted in the right panel of Fig. 7, in which we compare the observed and simulated pseudo-colour distributions. Indeed, the observed distribution (shown as a black line) is wider than the simulated one (red line); in particular, while the distributions are similar in the left half (i.e., blue side) of their respective profiles, the observed one extends towards a significantly redder colour than the simulated ones. The same results are obtained comparing the observed distribution with that obtained from the SYCLIST simulation (reported as a blue line in the right panel of Fig. 7). Hence, Fig. 7 suggests that the inclusion of gravity and limb darkening effects, as well as the inclusion of a random viewing angle, cannot account for the observed MSTO morphology, since the width and shape of the two simulated pseudo-colour distributions are almost identical.

To verify that the obtained results do not depend on the adopted age, in the top panels of Fig. 8, we compare the observed CMD with the other three SSP simulations which have older ages. The comparison between the observed and simulated pseudo-colour distributions for these SSPs is shown in the bottom panels. This comparison clearly shows that, as expected for older ages, the peak of the simulated distribution moves towards the right (i.e., towards redder colours), but, independently of the adopted age, the observed distribution is always wider than the simulated ones. Thus, it seems that a range of rotation velocities, which can

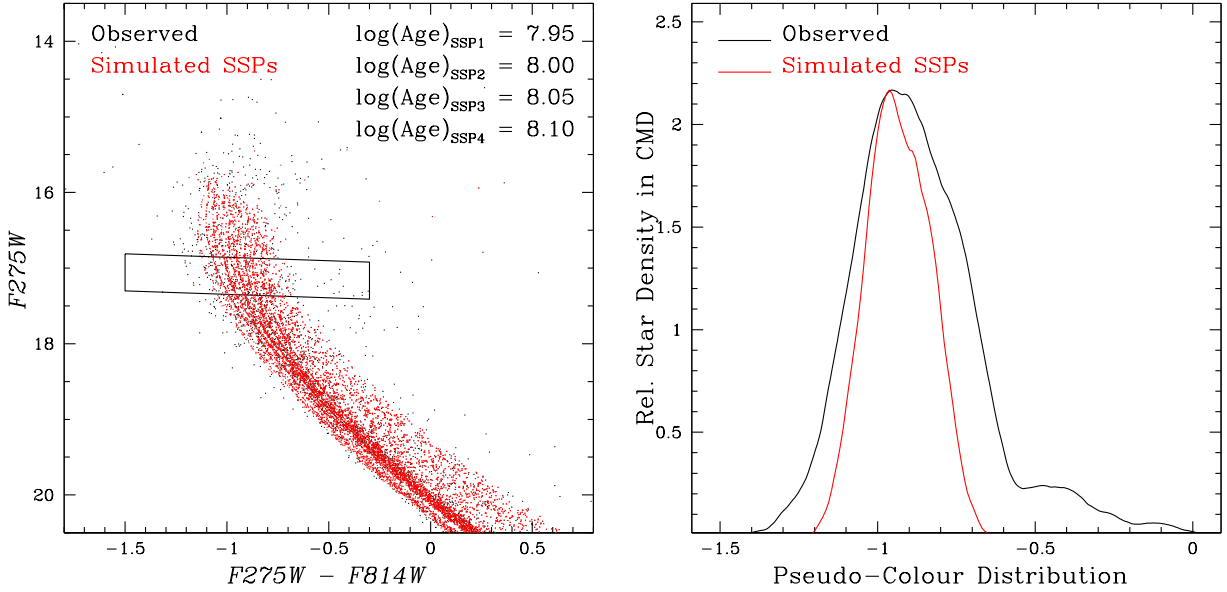


Figure 9. Left panel: comparison between observed (black dots) and simulated (red dots) CMDs. The latter is obtained combining four SSPs with different ages (~ 90 Myr, ~ 100 Myr, ~ 110 Myr, and ~ 125 Myr) and different rotation rates. Right panel: pseudo-colour distribution for the MSTO region of the observed (black line) and simulated (red line) CMDs.

reproduce the MS split, cannot explain the observed MSTO morphology.

5.2 Testing the combination of stellar rotation and age spread

In this context, we test the possibility that the *e*MSTO can be caused by a combination of the two effects, that is the presence of an age spread *and* a range of stellar rotation velocities for the cluster stars. To test this hypothesis, we derive the combined pseudo-colour distribution of the 4 SSPs. At this stage, we are only interested in verifying whether the combination of a range of SSP ages provide a pseudo-colour distribution width that can match the observed one, and not in a detailed comparison of their global profiles. Hence, we assume that the four SSPs have the same number of stars in the CMD, without tailoring the relative weights based on the observed profile. The left panel of Fig. 9 shows the comparison between the observed and simulated CMD, whereas in the right panel we plot the corresponding pseudo-colour distributions. The right panel clearly shows that the two distributions are similar and that their widths are comparable (see Sect. 6 below for a possible explanation of the discrepancy between the two distributions at the red end). It is also worth to note that the obtained distribution is not obviously bimodal and is well approximated by a single Gaussian. This indicates that the profile of the distribution itself cannot be used to exclude the presence of an age spread, in contradiction with the claims of Bastian et al. (2016)⁴.

⁴ It is premature to predict exactly when secondary star formation might have occurred after the first burst of star formation, since the gas input can in principle come from various sources (e.g., accreted “pristine” gas and/or slow winds from massive stars or AGB stars).

Hence, the results presented in these Sections show that a single SSP with different rotation rates fails in reproducing the observed pseudo-colour distribution of the MSTO whereas a combination of four SSPs with different ages and different rotation rates can provide a better fit. This suggests that both effects are necessary to reproduce the observed MSTO region morphology.

6 INSIGHTS FROM $H\alpha$ ANALYSIS

One of the original goals of this work was to determine whether NGC 1850 hosts *ongoing* star formation. Although the results from the analysis of the MSTO region presented in Sect. 4 and 5 seem to exclude such presence, a definitive answer can be provided by performing a search for pre-main sequence stars exploiting narrow-band imaging of the $H\alpha$ emission line.

To do this, we use the method adopted in C15 and described in detail in De Marchi et al. (2010).

The top panels of Fig. 10 show the $F467M - F656N$ vs. $F467M - F814W$ colour-colour diagram for the stars in the cluster field (top-left panel) and for the stars in the “control field” (top-right panel), the same field we used to derive the background contamination in Fig. 2. Using the median $F467M - F656N$ colour of stars with small photometric uncertainties in each of the three bands as a function of $F467M - F814W$, we define the reference sequence with respect to which $H\alpha$ emission excess is identified (shown as the dashed line in Fig. 10). To select a first candidate sample of stars with $H\alpha$ excess emission, we consider all those objects with a $F467M - F656N$ colour at least 5σ above the reference sequence, where σ is the uncertainty of the $F467M - F656N$ colour for each star. Then, we calculate the equivalent width of the $H\alpha$ emission line ($EW_{H\alpha}$) from the measured colour

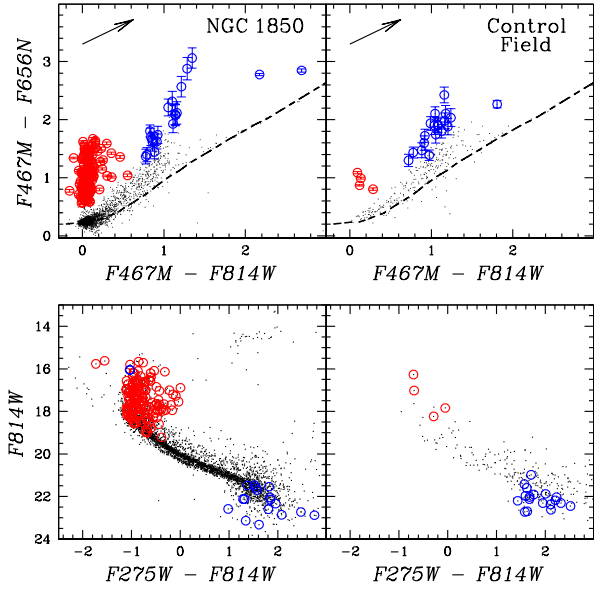


Figure 10. Top panels: $F_{467M} - F_{656N}$ vs. $F_{467M} - F_{814W}$ colour-colour diagram for the stars inside the NGC 1850 field (left panel) and in the control field (right panel), representing the contamination from the background LMC stars. The dashed line represents the median $F_{467M} - F_{656N}$ colour of stars with small photometric uncertainties in each of the three bands, representative of stars with no $H\alpha$ excess. $H\alpha$ -emitting stars that satisfy the criteria explained in Sect. 6 are shown as open red or blue circles, depending on their $F_{467M} - F_{814W}$ colour. Bottom panels: CMDs of the cluster (left panel) and of the control field (right panel). Stars with $H\alpha$ excess are shown as red or blue open circles as explained above.

excess, using the following equation from De Marchi et al. (2010):

$$EW_{H\alpha} = RW \times \left[1 - 10^{-0.4 \times (H\alpha - H\alpha^c)} \right] \quad (1)$$

where RW is the rectangular width of the filter, similar in definition to the equivalent width of the line (for the adopted F_{656N} filter, $RW = 27.61$; see Table 4 in De Marchi et al. 2010) and $H\alpha - H\alpha^c$ is the difference between the measured $H\alpha$ magnitude and the $H\alpha$ continuum, represented in this case by the difference between the star $F_{467M} - F_{656N}$ colour and the reference sequence $F_{467M} - F_{656N}$ colour, at the corresponding $F_{467M} - F_{814W}$. Finally, we keep only the objects for which $EW_{H\alpha} > 10 \text{ \AA}$ (White & Basri 2003). The stars that satisfy these criteria are reported as red or blue open circles in Fig. 10, depending on their $F_{467M} - F_{814W}$ colour.

The top panels of Fig. 10 show that for $F_{467M} - F_{814W} \gtrsim 0.7$ mag, the number of stars with $H\alpha$ excess is similar in both fields (blue open circles). However, there is a large number of objects in the NGC 1850 field with $F_{467M} - F_{814W} \approx 0.0 - 0.2$ mag (see red open circles), for which there is almost no counterpart in the control field (only four objects). In the lower panels of Fig. 10, we superimpose these objects on the F_{814W} vs. $F_{275W} - F_{814W}$ CMDs. Note that they are located in the MSTO region, covering its whole extension. In particular, we derive that in the parallelogram box used to

select MSTO stars in the previous Sections, they represent almost the 40% of the total number of stars. The presence of $H\alpha$ excess in stars with absolute magnitude $M_{F_{814W}} \sim -1$ suggests that these objects are Be stars. The emission lines from these stars arise due to ionized circumstellar material ejected along the poles of rapidly rotating B stars at $\Omega/\Omega_{crit} \gtrsim 0.5$ (e.g., Stee & Meilland 2009). Pending spectroscopic confirmation of these objects as Be stars, these results constitute direct evidence that NGC 1850 hosts a significant number of fast-rotating stars. In particular, we note that around $-0.5 \lesssim F_{275W} - F_{814W} \lesssim -0.1$ and $F_{814W} \sim 18$ mag, there is a group of stars with $H\alpha$ excess, which are clearly redder than the majority of stars populating the MSTO region. We suggest that this may be due to the presence of a dusty circumstellar disk that is oriented in a close to edge-on configuration, thus providing a “local” source of reddening that cannot be corrected using the differential dereddening technique adopted in this work.

To test whether these objects may be responsible for the discrepancy between the observed pseudo-colour distribution and the simulated one (cf. Sect. 5.2), we adopt the following empirical approach. We remove all stars that show an $H\alpha$ excess (independently of the derived equivalent widths) from our NGC 1850 catalog. In Fig. 11 we show the comparison between the observed CMD (left panel) and the one obtained after the stars with $H\alpha$ excess are removed from our sample (right panel). For comparison purposes, we also superimpose onto both CMDs the same simulated single-age CMD as in Fig. 7 (shown as red dots). As Fig. 11 clearly shows, the removal of $H\alpha$ -emitting stars results in the removal of almost all stars that were significantly redder than, and detached from, the MSTO. Then, we derive the pseudo-colour distribution for this subset of stars and compare it with the original one. This comparison is shown in Fig. 12. Note that the red tail of the original distribution with pseudo-colour $\gtrsim -0.5$ mag is absent in the new one, which is also somewhat narrower than the original one. However, the comparison with the simulated single-age pseudo-colour distribution (red line in Fig. 12) shows that the latter is still significantly narrower than the observed distribution. We also show in Fig. 12 the pseudo-colour distribution obtained from the combination of four simulated SSPs (represented by the red dashed line). In this case, the simulated distribution provides a good match to the observed one, better in fact than the original observed one that included the Be stars (cf. Sect. 5.2). However, we note that a small discrepancy still persists at the red end of the distribution. This seems to indicate that an even older population can be present in the cluster and that the derived age spread of ~ 35 Myr can be considered as a lower limit.

These results strongly suggest that the population of $H\alpha$ -emitting stars in the MSTO region cannot account alone for the difference between the observed pseudo-colour distributions and those of the single-age simulations, confirming that rotation alone cannot produce the observed morphology of the eMSTO.

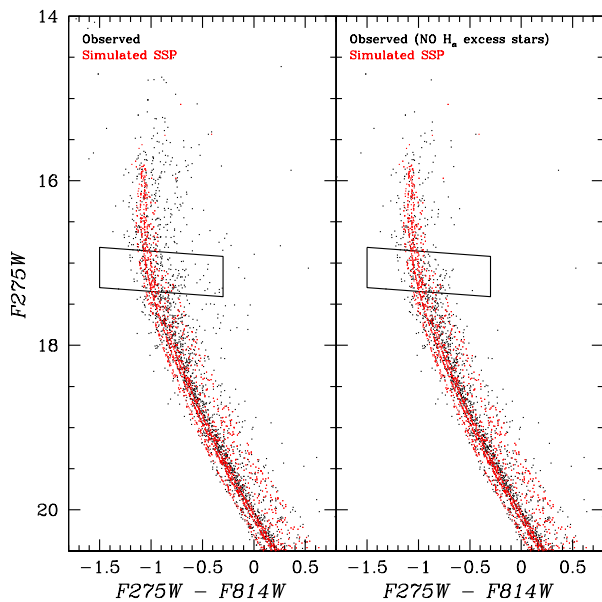


Figure 11. Comparison between the observed CMD (left panel) and the one obtained after removing all stars that show an H α excess (right panel). In both panels we overplot (red dots) the CMD obtained from the Monte Carlo simulations of a SSP (the same as in Fig. 7). The parallelogram used to obtain the pseudo-colour distribution is also shown.

7 INSIGHTS FROM THE RADIAL DISTRIBUTION OF THE TWO MS POPULATIONS

To investigate whether the population ratio between the two MSes (i.e., between non-rotating or slow-rotating and fast-rotating stars) changes as a function of cluster-centric radius we use the following method. First, we compute a fiducial line for the blue and red MS and we derive the verticalized CMD in such a way that the blue and the red fiducial translate into vertical line with abscissa 0 and 1, respectively (Milone et al. 2015b). To do this we define for each star $\Delta_{col}^N = [(col - col_{blue\,fiducial}) / (col_{red\,fiducial} - col_{blue\,fiducial})]$, where col is $F275W - F814W$. This particular CMD allows to separate the two MSes from each other and from the binary sequence more clearly.

We focus our analysis in the magnitude interval $19.5 < F814W < 21.0$ mag. In particular, the lower magnitude limit has been chosen to exclude the faint part of the two MSes, where they seem to merge together and thus the separation is not clear. Finally, we derive the distribution of stars perpendicular to the MS in five cluster-centric annuli, chosen in such a way that they contain the same number of stars. In the inset of Fig. 13 we show an example of the observed histogram distribution for the third radial interval. We applied a smoothed naïve estimator (Silverman 1986) to be insensitive to a particular binning starting point. To determine the fraction of blue MS stars with respect to the total number of stars in each region, we adopt a Δ_{col}^N cut in the observed histogram distribution: stars with $\Delta_{col}^N < 0.35$ mag are associated to the blue MS, whereas stars with $0.35 < \Delta_{col}^N < 1.5$ mag are associated to the red MS (the two limits are

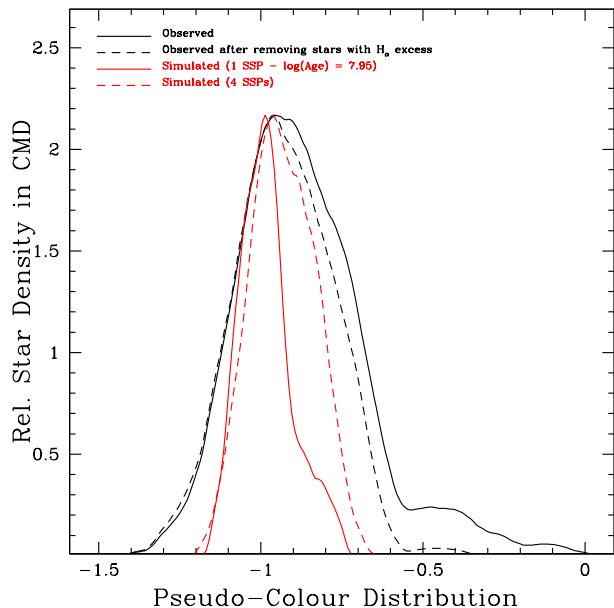


Figure 12. Comparison between the observed pseudo-colour distribution obtained from all the stars in the MSTO region (black line), the one obtained after removing the sample the stars with H α excess (dashed black line), the one derived from a SSP (red line), and the one derived from the combination of four SSPs (dashed red line).

reported in Fig. 13 as dashed lines). The latter Δ_{col}^N limit has been chosen to avoid the contamination from binary stars.

In Fig. 13, we show the fraction of blue MS stars with respect to the total number of MS stars as a function of the radial distance from the cluster center. Fig. 13 shows that this ratio is constant with radius to within the Poisson uncertainties. To test the robustness of this result, we also adopt a different method to derive the fraction of blue and red MS stars in the different cluster-centric annuli. We use a bi-Gaussian function to fit the observed histogram distribution by means of least squares and we infer the fraction of stars in each MS from the areas under the Gaussians. The results obtained from the two different methods are consistent within the errors.

Taken these results at face value, it seems that the non-rotating/slow-rotating and fast-rotating stars share the same radial distribution. Recently, similar studies have been carried out for other two young star clusters: Li et al. (2016) studied NGC 1856 and found similar results to ours for NGC 1850, that is the two populations share the same radial distribution, whereas in the cluster NGC 1866, Milone et al. (2016b) did find a difference in the radial distribution, with the fraction of non-rotating/slow-rotating stars (blue MS) increasing slowly outward beyond its effective radius. On the other hand, Goudfrooij et al. (2011b) determined the radial distribution of eMSTO stars in several intermediate-age (1–2 Gyr) massive star clusters. They find that, for the clusters with the highest escape velocities and longest relaxation times, the stars in the brightest half of the MSTO region are significantly more centrally concentrated than the stars in the faintest half. This has been interpreted in terms of an age spread; the indication that the inner region of the clus-

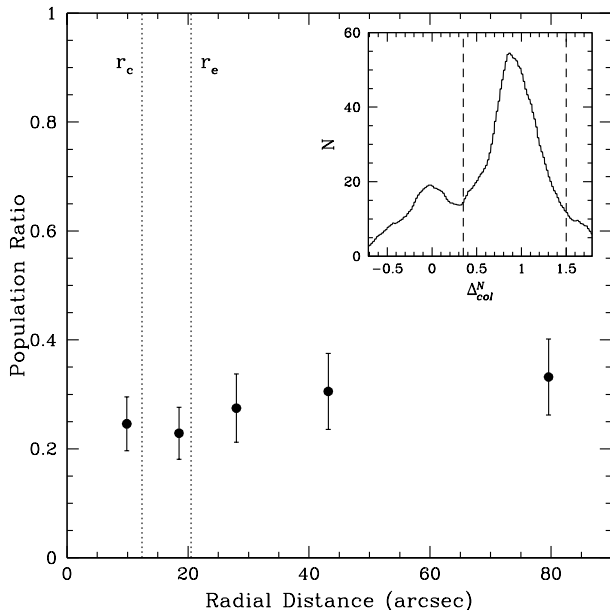


Figure 13. Fraction of blue-MS stars with respect to the total number of MS stars as a function of the radial distance from the cluster center (in arcsec). The dotted vertical lines mark the projected core and effective radius. The inset panel shows the observed histogram distribution for the third radial interval. The ΔN_{col}^N limits adopted to associate stars to the red and blue MS are reported as dashed lines.

ter are preferentially populated by second-generation stars is in agreement with the prediction of the *in situ* scenario (D’Ercole et al. 2008). Hence, if we assume that the results obtained here are valid also for intermediate-age star clusters (i.e., non-rotating and fast-rotating stars have the same radial distributions), it seems highly unlikely that the observed different central concentration can be explained in terms of a range of rotation velocities in the massive intermediate-age clusters. This suggests that the eMSTO phenomenon in intermediate-age star clusters may be due, at least in part, by a spread in age. Unfortunately, a direct comparison with the radial distribution of MSTO stars in NGC 1850 is hampered by the low number of objects in the cluster MSTO region.

8 INSIGHTS FROM DYNAMICAL ANALYSIS

One of the important features of the eMSTO phenomenon in intermediate-age star clusters in the Magellanic Clouds is that they do not occur in *all* such clusters. A possible explanation of this in the context of multiple populations was provided by Goudfrooij et al. (2011a), who suggested that eMSTO are only hosted by clusters whose escape velocities were higher than the wind velocities of first-generation “polluters” stars that are thought to provide the seed material for secondary star formation, during the era when the cluster contained such stars (this is referred to as the “early escape velocity threshold” scenario). The most popular types of such polluter stars are (i) AGB stars with $4 \lesssim M/M_{\odot} \lesssim 8$ (D’Antona & Ventura 2008), (ii) massive rotating stars (“FRMS”, Decressin et al. 2007), and (iii) mas-

sive binary stars (de Mink et al. 2009). Subsequently, the studies of Goudfrooij et al. (2014) and Correnti et al. (2014) suggested that the critical escape velocity⁵ for a star cluster to be able to retain the material ejected by first-generation polluter stars seem to be in the range of 12–15 km s^{−1}.

Furthermore, the calculations of Conroy & Spergel (2011) show that massive clusters should be able to sweep up significant fractions of their mass from the ambient interstellar medium (ISM) at young ages if their environment is sufficiently conducive. Under the assumptions that (1) the line-of-sight velocity dispersion of the LMC ($\sigma \sim 20$ km s^{−1}, van der Marel et al. 2002) is a typical relative velocity between a star cluster and the ambient ISM in the LMC, and (2) a typical young cluster in the LMC has a half-mass radius of ≈ 5 pc (Mackey & Gilmore 2003; C15), equations 5–8 of Conroy & Spergel (2011) suggest that this can occur in the present-day LMC if the cluster is massive enough ($M \gtrsim 10^5 M_{\odot}$) and the local ISM is dense enough but not so dense that it would strip any gas accreted by the cluster by ram pressure in its orbit ($1 \lesssim (n/\text{cm}^3) \lesssim 100$ for a $10^5 M_{\odot}$ cluster).

With this in mind, we determine the structural and dynamical parameters of the cluster as described below.

8.1 Structural parameters

To determine the radial surface number density distribution of stars, we follow the procedure described by Goudfrooij et al. (2009) and adopted in C15.

We fit the radial surface number density profile using a King (1962) model combined with a constant background level, described by the following equation:

$$n(r) = n_0 \left(\frac{1}{\sqrt{1 + (r/r_c)^2}} - \frac{1}{\sqrt{1 + c^2}} \right)^2 + \text{bkg} \quad (2)$$

where n_0 is the central surface number density, r_c is the core radius, $c \equiv r_t/r_c$ is the King concentration index (r_t being the tidal radius), and r is the equivalent radius of the ellipse ($r = a\sqrt{1 - \epsilon}$, where a is the semi-major axis of the ellipse and ϵ is its ellipticity). Fig. 14 shows the best-fit King model, obtained using a χ^2 minimization routine. The derived core radius $r_c = 12''.4 \pm 0''.5$, which corresponds to 3.01 ± 0.12 pc, whereas the effective radius $r_e = 20''.5 \pm 1''.4$ (4.97 ± 0.35 pc). Our estimate for r_c is in reasonable agreement with the 2.7 pc derived by Niederhofer et al. (2015).

8.2 Cluster mass and escape velocity

We estimate the cluster mass and escape velocity as a function of time going back to an age of 10 Myr, after the cluster has survived the era of violent relaxation and when the most massive stars of the first generation that are proposed to be candidate polluters in literature (i.e. FRMS and massive binary stars), are expected to start losing significant amounts of mass through slow winds.

The current mass of NGC 1850 is determined from its integrated-light *I*-band magnitude listed in Table 1 and derived as described in C15. In this particular case, in order

⁵ Note that these studies used a Salpeter IMF for mass determination.

Cluster (1)	I (2)	Aper. (3)	Aper. Corr. (4)	[Z/H] (5)	A_V (6)	r_c (7)	r_e (8)	$\log(M_{cl}/M_\odot)$ (9)	$\log(M_{cl}/M_\odot)$ (10)
NGC 1850	9.43 ± 0.04	20	0.47 ± 0.03	-0.3	0.372	3.01 ± 0.12	4.97 ± 0.35	4.86 ± 0.10	4.62 ± 0.10

Table 1. Physical properties of the star cluster. Columns (1): Name of the cluster. (2): Integrated V magnitude. (3): Adopted radius in arcsec for the measure of the integrated magnitude. (4): Aperture correction in magnitude. (5): Metallicity (dex). (6): Visual extinction A_V in magnitude. (7): Core radius r_c in pc. (8): Effective radius r_e in pc. (9-10): Logarithm of the cluster mass adopting a [Salpeter \(1955\)](#) and a [Chabrier \(2003\)](#) initial mass function, respectively.

to minimize the contamination by NGC 1850B, we derive the aperture-photometry magnitudes of stars inside a radius of $20''$, centered at the coordinates found in the analysis of Sect. 8.1, measured on the *F814W drc* image (obtained combining long and short exposures). The background level and its uncertainty is derived from five different regions of the image with distances larger than $100''$ from the center of NGC 1850, avoiding the major $H\alpha$ emission filaments (see Fig. 1).

We calculate the escape velocity of NGC 1850 and its evolution with time using the prescriptions of [Goudfrooij et al. \(2014\)](#). Briefly, we evaluate the evolution of cluster mass and radius with and without mass segregation. This property plays a fundamental role in terms of the early evolution of the cluster’s expansion and mass-loss rate (e.g., [Mackey et al. 2008b](#); [Vesperini et al. 2009](#)). For the case of a model cluster with initial mass segregation, we adopt the results of the simulation called SG-R1 in [D’Ercole et al. \(2008\)](#), which involves a model cluster that features a level of initial mass segregation of $r_e/r_{e,>1} = 1.5$, where $r_{e,>1}$ is the effective radius of the cluster for stars with $M > 1 M_\odot$ (see [Goudfrooij et al. 2014](#), for a detailed description of the reasons for this choice). Escape velocities are calculated from the reduced gravitational potential $V_{\text{esc}}(r, t) = (2\Phi_{\text{tid}}(t) - 2\Phi(r, t))^{1/2}$, at the core radius and at the effective radius. We choose to calculate the escape velocity at the cluster core radius in accordance with the prediction of the *in situ* scenario ([D’Ercole et al. 2008](#)), where the second generation stars are formed in the innermost region of the cluster. Assuming a [Salpeter \(1955\)](#) initial mass function, the current cluster escape velocity is $10.5 \pm 0.2 \text{ km s}^{-1}$ at the effective radius and $13.8 \pm 0.2 \text{ km s}^{-1}$ at the core radius. For a [Chabrier \(2003\)](#) initial mass function, we obtain $8.0 \pm 0.2 \text{ km s}^{-1}$ and $10.6 \pm 0.2 \text{ km s}^{-1}$, respectively.

Fig. 15 shows the “plausible” escape velocity of NGC 1850 as a function of time (black line), derived using the same approach as in C15 and described in detail in [Goudfrooij et al. \(2014\)](#), for a [Salpeter \(1955\)](#) initial mass function. Briefly, the “plausible” escape velocity is calculated adopting a procedure that takes into account the various results from the compilation of Magellanic Cloud star cluster properties and N-body simulations by [Mackey et al. \(2008b\)](#).

For comparison Fig. 15 also shows the escape velocity as a function of time for the limiting cases in which (1) the cluster does not have any primordial mass segregation (blue line) and (2) the cluster has the same level of primordial mass segregation as the model SG-R1 by [D’Ercole et al. \(2008\)](#), (red line). The critical escape velocity range of $12 - 15 \text{ km s}^{-1}$ is depicted as the light grey region in Fig. 15, whereas

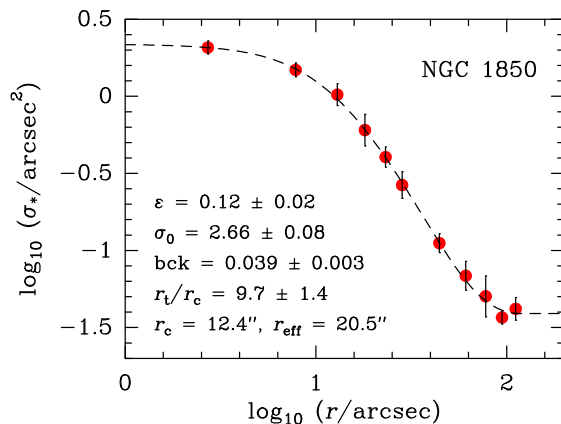


Figure 14. Radial surface number density profile of NGC 1850. Red points represent observed values. The dashed line represents the best-fit King model (cf. equation 2) whose parameters are shown in the legend. Ellipticity and effective radius r_e are also shown in the legend.

the region below 12 km s^{-1} , representing the velocity range in which eMSTOs are not observed in LMC star clusters, is shown in dark grey.

Fig. 15 shows that, independent of the assumed level of primordial mass segregation in the cluster, the initial escape velocity was likely high enough to retain the material ejected through winds by the first-generation polluters. Moreover, it seems to decrease below the critical value of $\sim 15 \text{ km s}^{-1}$ at an age similar to what we derive as the age spread (i.e., 30–40 Myr)⁷. In the context of the *in situ* scenario, considering the time when first-generation polluters are predicted to be present in the cluster (i.e., at ages of $\sim 5 - 30$ Myr for massive stars and $\sim 50 - 200$ Myr for IM-AGB stars) and the age ranges derived from our analysis (i.e., 30–40 Myr), it seems that massive stars would be the most likely source of “polluted” material in NGC 1850. Future investigations of the range of light-element abundances (e.g., Na or N) found in NGC 1850 should be able to shed more light on the extent to which the cluster has actually retained such polluted material. Furthermore, the mass of NGC 1850 is high enough for the cluster to have been able to accrete a significant amount of “pristine” gas from its surroundings in the past, which could have constituted an additional source of gas to form stars after the initial burst that formed NGC 1850 (cf. above;

⁷ We emphasize that the critical value 15 km s^{-1} (for a Salpeter IMF) was not more than a best-effort estimate by [Goudfrooij et al. \(2014\)](#) based on empirical data, and should not be interpreted as a precise number.

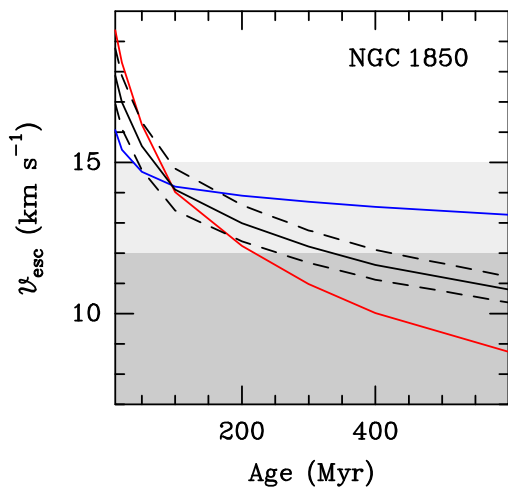


Figure 15. Escape velocity as a function of time at the core radius. The black curve represents the “plausible” escape velocity, derived as described in Sect. 8.2. Formal $\pm 1 \sigma$ errors of V_{esc} are shown by the dashed line. The blue line represents the escape velocity in case NGC 1850 had no primordial mass segregation, while the red line does so in case it had the same level of primordial mass segregation as the model SG-R1 in D’Ercole et al. (2008). The light grey region represents the critical range of V_{esc} mentioned in Sect. 8, i.e. $12\text{--}15 \text{ km s}^{-1}$. The region below 12 km s^{-1} in which V_{esc} is thought to be too low to permit retention of material shed by the first stellar generation, is shaded in dark grey.

Conroy & Spergel 2011; Goudfrooij et al. 2014; but see also Bastian & Strader 2014).

9 SUMMARY AND CONCLUSIONS

We present the results of a study of new, deep *HST* WFC3 images of the young (~ 100 Myr) star cluster NGC 1850 in the LMC. The analysis of its CMD reveal the presence of an eMSTO and a double MS. The blue component of the MS hosts about a quarter of the the total number of MS stars. We verify that these features cannot be explained in terms of photometric errors, contamination from background LMC stars, or differential reddening.

From a comparison with theoretical models, we show that the MS split cannot be reproduced using non-rotating isochrones with different ages. Conversely, it is very well reproduced by a coeval stellar population with a variety of rotation rates. However, when adopting the latter models, we show that the observed morphology of the MSTO cannot be fit satisfactorily: the pseudo-colour distribution of stars across the MSTO obtained from the observed CMD is significantly wider than that obtained from Monte Carlo simulations of the set of single-age isochrones with a range of rotation rates that fit the double MS feature. A combination of SSPs with an age range of ~ 35 Myr *along with* different rotation rates reproduces the data significantly better.

From an analysis of narrow-band $H\alpha$ imaging, we find that the MSTO region hosts a population of Be stars, providing direct evidence that rapidly rotating stars are present in the cluster. We note that a fraction of these stars are redder than the majority of TO stars. We interpret this in

terms of an (close to) edge-on configuration of dusty circumstellar disks of Be stars, thus providing a source of local reddening that cannot be accounted for in our differential reddening correction. We quantify how this effect impacts the observed pseudo-colour distribution by removing all the stars with an $H\alpha$ excess from the original catalog and deriving a new pseudo-colour distribution. We demonstrate that this newly derived pseudo-colour distribution is still significantly wider than the simulated one. As such, the eMSTO morphology still cannot be explained by an SSP with a variety of stellar rotation rates; a spread of ages still seems to be required.

Finally, the dynamical properties of NGC 1850 derived from our data show that the cluster had an escape velocity within its core radius of $\sim 13\text{--}17 \text{ km s}^{-1}$, at an age of ~ 10 Myr, high enough in principle to retain material shed by the slow winds of “polluter stars”. Furthermore its mass was high enough to accrete “pristine” gas that may have been present in the environment of the cluster shortly after it was first formed.

The important role that stellar rotation can play in the interpretation of the eMSTO phenomenon in young and intermediate-age star clusters has been acknowledged in the recent literature, including in works that suggested that an age spread is responsible for eMSTOs (see for example C15 and Fig. 7 in Goudfrooij et al. 2014, and discussion therein). Unfortunately, the current lack of rotating isochrone models for masses $M < 1.7 M_{\odot}$ prevents us from testing in detail its impact in intermediate-age star clusters. At the same time, the new findings for the young clusters do not yet provide a significant clarification of the picture in terms of the role of stellar rotation in the eMSTO phenomenon. For example, Niederhofer et al. (2015) concluded that the eMSTO of intermediate-age star clusters can in principle be explained in terms of stellar rotation, as long as the initial rotation distribution covers the interval from $\Omega/\Omega_{crit} \sim 0.0$ to ≈ 0.5 . Conversely, the detailed studies of the split MS of NGC 1850 and other young clusters show that they can be reproduced only when assuming that a large number of stars are *fast* rotators (i.e., $\Omega/\Omega_{crit} \gtrsim 0.80$). Another open issue is the origin of the non-rotating or slow-rotating stellar populations (see Milone et al. 2016a, for a detailed discussion). Zorec & Royer (2012) suggested that the observed slow-rotating and non-rotating stars could have lost their angular momentum during the pre-MS phase do to magnetic breaking. An alternative hypothesis is that tidal interaction in binary systems could be responsible for slowing down a fraction of stars. In this context, D’Antona et al. (2015) suggested that binary synchronization could be responsible for the slow-rotating population.

Spectroscopic studies of the distribution of stellar rotation rates in young and intermediate-age star clusters will be of fundamental importance to test the aforementioned scenarios and address the role of the stellar rotation in the eMSTO phenomenon.

ACKNOWLEDGMENTS

Support for this project was provided by NASA through grant HST-GO-14174 from the Space Telescope Science Institute, which is operated by the Association of Universi-

ties for Research in Astronomy, Inc., under NASA contract NAS5-26555. We made significant use of the SAO/NASA Astrophysics Data System during this project. THP acknowledges support by the FONDECYT Regular Project Grant (n. 1161817) and the BASAL center for Astrophysics and Associated Technologies (PFB-06).

REFERENCES

- Anderson, J., et al. 2008, *AJ*, 135, 2055
- Bastian, N., & de Mink, S. E. 2009, *MNRAS*, 398, L11
- Bastian, N., et al. 2016, *MNRAS*, 460, L20
- Bastian, N., & Strader, J. 2014, *MNRAS*, 443, 3594
- Bellini, A., Anderson, J., & Bedin, L. R. 2011, *PASP*, 123, 622
- Bellini, A., et al. 2014, *ApJ*, 797, 115
- Brandt, T. D., & Huang, C. X. 2015, *ApJ*, 807, 24
- Bressan, A., Marigo, P., Girardi, L., Salasnich, B., Dal Cero, C., Rubele, S., & Nanni, A. 2012, *MNRAS*, 427, 127
- Bruzual, G. A., & Charlot, S. 2003, *MNRAS*, 344, 1000
- Chabrier, G. 2003, *PASP*, 115, 763
- Claret, A. 2000, *A&A*, 363, 1081
- Conroy, C., & Spergel, D. N. 2011, *ApJ*, 726, 36
- Correnti, M., Goudfrooij, P., Puzia, T. H., & de Mink, S. E. 2015, *MNRAS*, 450, 3054
- Correnti, M., Goudfrooij, P., Kalirai, J. S., Girardi, L., Puzia, T. H., & Kerber, L. 2014, *ApJ*, 793, 121
- D’Antona, F., Di Criscienzo, M., Decressin, T., Milone, A. P., Vesperini, E., & Ventura, P. 2015, *MNRAS*, 453, 2637
- D’Antona, F., & Ventura, P. 2008, *MNRAS*, 479, 805
- Decressin, T., Meynet, G., Charbonnel, C., Prantzos, N., & Ekström, S. 2007, *A&A*, 464, 1029
- de Mink, S. E., Pols, O. R., Langer, N., & Izzard, R. G. 2009, *A&A*, 5007, L1
- De Marchi, G., Panagia, N., & Romaniello, M. 2010, *ApJ*, 715, 1
- D’Ercole, A., Vesperini, E., D’Antona, F., McMillan, S. L. W., & Recchi, S. 2008, *MNRAS*, 391, 825
- Ekström, S., et al. 2012, *A&A*, 537, 146
- Espinosa Lara, F., & Rieutord, M. 2011, *A&A*, 533, 43
- Feigelson, E. D., & Montmerle, T. 1999, *ARA&A*, 37, 363
- Georgy, C., Ekström, S., Granada, A., Meynet, G., Mowlavi, N., Eggenberger, P., & Mader, A. 2013, *A&A*, 553, 24
- Georgy, C., Granada, A., Ekström, S., Meynet, G., Anderson, R. I., Wyttenbach, A., Eggenberger, P., & Mader, A. 2014, *A&A*, 566, 21
- Gilliland, R. L., 2004, ACS/ISR 2004-01 (Baltimore, MD: STScI), available online at <http://www.stsci.edu/hst/acs/documents/isrs>
- Gilliland, R. L., Rajan, A., & Deustua, S. 2010, WFC3/ISR 2010-10 (Baltimore, MD: STScI), available online at <http://www.stsci.edu/hst/efc3/documents/isrs>
- Girardi, L., Eggenberger, P., & Miglio, A. 2011, *MNRAS*, 412, L10
- Girardi, L., Rubele, S., & Kerber, L. 2009, *MNRAS*, 394, L74
- Glatt, K. et al., 2008, *AJ*, 135, 1703
- Goudfrooij, P., Puzia, T. H., Kozhurina-Platais, V., & Chandar, R. 2009, *AJ*, 137, 4988
- Goudfrooij, P., Puzia, T. H., Chandar, R., & Kozhurina-Platais, V. 2011, *ApJ*, 737, 4 (G11a)
- Goudfrooij, P., Puzia, T. H., Kozhurina-Platais, V., & Chandar, R. 2011, *ApJ*, 737, 3 (G11b)
- Goudfrooij, P., et al. 2014, *ApJ*, 797, 35
- Huang, W., Gies, D. R., & McSwain, M. V. 2010, *ApJ*, 722, 605
- Keller, S. C., Mackey, A. D., & Da Costa, G. S. 2012, *ApJ*, 761, L5
- King, I. 1962, *AJ*, 67, 471
- Li, Z., Mao, C., Chen, L., & Zhang, Q. 2012, *ApJ*, 761, 22
- Li, C, de Grijs, R, Deng, L., & Milone, A. P. 2016, arXiv161104659
- Mackey, A. D., Broby Nielsen, P., Ferguson, A. M. N., & Richardson, J. C. 2008, *ApJ*, 681, L17
- Mackey, A. D., & Gilmore, G. F. 2003, *MNRAS*, 338, 85
- Mackey, A. D., Wilkinson, M. I., Davies, M. B., & Gilmore, G. F. 2008, *MNRAS*, 386, 65
- Milone, A. P., Bedin, L. R., Piotto, G., & Anderson, J. 2009, *A&A*, 497, 755
- Milone, A. P., et al. 2012, *A&A*, 537, 77
- Milone, A. P., et al. 2013, *A&A*, 555, 143
- Milone, A. P., et al. 2015a, *MNRAS*, 450, 3750
- Milone, A. P., et al. 2015b, *ApJ*, 808, 51
- Milone, A. P., Marino, A. F., D’Antona, F., Bedin, L. R., Da Costa, G. S., Jerjen, H., & Mackey, A. D. 2016, *MNRAS*, 458, 4368
- Milone, A. P., et al. 2016, arXiv161106752
- Mowlavi, N., Eggenberger, P., Meynet, G., Ekström, S., Georgy, C., Mader, A., Charbonnel, C., & Eyer, L., 2012, *A&A*, 541, 41
- Niederhofer, F., Hilker, M., Bastian, N., & Silva-Villa, E. 2015, *A&A*, 575, 62
- Royer, F., Zorec, J., & Gomez, A. E. 2007, *A&A*, 463, 671
- Rubele, S., Girardi, L., Kozhurina-Platais, V., Goudfrooij, P., & Kerber, L. 2011, *MNRAS*, 414, 2204
- Rubele, S., Kerber, L., & Girardi, L. 2010, *MNRAS*, 403, 1156
- Salpeter, E. E. 1955, *ApJ*, 121, 161
- Silverman, B. W. 1986, in *Density Estimation for Statistics and Data Analysis*, Chap and Hall/CRC Press, Inc.
- Stee, P., & Meilland, A. 2009, in *The Rotation of Sun and Stars*, Lecture Notes in Physics, 765, 195
- van der Marel, R. P., Alves, D. R., Hardy, E., & Suntzeff, N. B. 2002, *AJ*, 124, 2639
- Vesperini, E., McMillan, S. L. W., & Portegies Zwart, S. 2009, *ApJ*, 698, 615
- White, R. J., & Basri, G. 2003, *ApJ*, 582, 1109
- Yang, W., Meng, X., Bi, S., Tian, Z., Li, T., & Liu, K. 2011, *ApJ*, 731, L37
- Yang, W., Bi, S., Meng, X., & Liu, Z. 2013, *ApJ*, 776, 112
- Zorec, J., & Royer, F. 2012, *A&A*, 537, 120